Shear Modulus Estimation With Vibrating Needle Stimulation

Marko Orescanin, *Student Member, IEEE*, and Michael F. Insana, *Senior Member, IEEE*

***Abstract*—An ultrasonic shear wave imaging technique is being developed for estimating the complex shear modulus of biphasic hydropolymers including soft biological tissues. A needle placed in the medium is vibrated along its axis to generate harmonic shear waves. Doppler pulses synchronously track particle motion to estimate shear wave propagation speed. Velocity estimation is improved by implementing a k-lag phase estimator. Fitting shear-wave speed estimates to the predicted dispersion relation curves obtained from two rheological models, we estimate the elastic and viscous components of the complex shear modulus. The dispersion equation estimated using the standard linear solid-body (Zener) model is compared with that from the Kelvin-Voigt model to estimate moduli in gelatin gels in the 50 to 450 Hz shear wave frequency bandwidth. Both models give comparable estimates that agree with independent shear rheometer measurements obtained at lower strain rates.**

I. Introduction

Three-dimensional hydrated collagen and agarose scaffolds are now standard media for exploring cellular mechanobiology [1]–[3]. Embedded cells respond to their mechanical environment as provided by the support matrix, which in breast tissue determines many cell functions from normal homeostatic behavior through malignant cell progression, tumor growth, and metastasis. Consequently, deformation patterns of these fluidic polymers reveal essential properties of the mechano-environment that regulate mammary cell behavior. Three-dimensional cell cultures are ideal media for discovering biological sources of elasticity image contrast that can be related back to the cellular biology of the underlying disease process. We are developing verifiable techniques for measuring viscoelastic properties of 3-D cell culture gels under sterile conditions and over an extended applied-force bandwidth.

During the last decade, several shear-wave estimation techniques have emerged as tools for measuring mechanical moduli of biological tissues [4]–[12]. These dynamic techniques apply an acoustic radiation force or contact vibrator to generate shear waves in the medium that are imaged by phase-sensitive medical imaging methods, e.g., ultrasonic, magnetic resonance (MR), or optical. We describe an ultrasonic Doppler technique that maps shear wave energy generated by a vibrating needle at frequencies between 50 and 450 Hz to estimate viscoelastic parameters. It builds on a growing shear-wave imaging literature for estimating the regional elastic modulus [13], [14].

A mechanical actuator harmonically drives a stainless steel needle placed in the medium to generate narrow-band cylindrical shear waves. Shear waves are imaged in a radial plane using a multi-lag phase estimator, which leverages the narrow-band wave feature to extend standard pulse-pair (lag-one) processing for reduced velocity variance. Performance of the multi-lag phase estimator is evaluated experimentally and through simulation. We use a phase-gradient technique to estimate shear wave speed from estimated particle velocities at each frequency, and we fit those results to rheological model predictions relating shear wave dispersion to the complex modulus of the medium. Thus, we obtain spatially-averaged modulus estimates for hydrogel media that can be independently verified to assess accuracy and precision.

II. Methods

The aim of the proposed method is to accurately measure the complex shear modulus of soft biological media. These initial studies measure properties of collagenous hydrogels that share key structural and mechanical features of natural and engineered breast tissues [15].

A. Temporal Phase and Velocity Estimation

The shear wave imaging experiment is depicted in Fig. 1. A mechanical actuator (SF-9324, PASCO Scientific, Roseville, CA) was adapted to hold a stainless-steel needle. The needle is 1.5 mm in diameter (17 gauge) and 13 cm long. The actuator is driven by an arbitrary waveform generator transmitting 500 ms pure-tone voltage bursts in the frequency range of 50 to 450 Hz. The voltage amplitude ranged from 5 to 15 V. The needle vibrates along the z-axis, thus generating cylindrical shear waves that propagate radially for several millimeters. Harmonic shear waves are tracked with a linear-array transducer (BW-14/60, SonixRP, Ultrasonix Medical Corp., Richmond, BC, Canada). The axis of the vibrating needle is oriented $\theta = 35 \pm 5°$ from the Doppler beam axis.

The ultrasound system was used to estimate particle velocity via pulsed Doppler methods. A linear array transducer driven by 6-cycle, 6.67-MHz voltage pulses gen-

Manuscript received December 28, 2009; accepted February 19, 2010. We gratefully acknowledge the support of Dr. L. Huang and the U.S. Department of Energy through the LANL/LDRD Program for this work. This work was supported in part by the National Cancer Institute under award number R01 CA082497.

The authors are with the Department of Electrical and Computer Engineering and the Beckman Institute for Advanced Science and Technology at the University of Illinois at Urbana-Champaign, Urbana, IL (e-mail: moresca2@illinois.edu).

M. F. Insana is also with the Department of Bioengineering at the University of Illinois at Urbana-Champaign, Urbana, IL.

Digital Object Identifier 10.1109/TUFFC.2010.1555

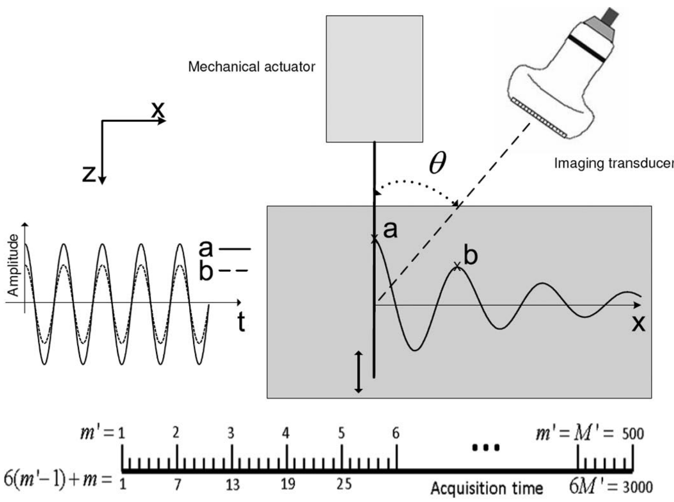

Fig. 1. Diagram of the experiment to measure viscoelastic properties of gel samples. Mechanical actuator is driving a stainless steel needle. Momentum of the needle displacement is transferred to the medium as cylindrical shear waves. A linear array Doppler probe tracks the induced transverse motion of scatterers as shear waves propagate. At the bottom is a timing diagram for the (up to) 3000 Doppler pulses transmitted at each position along x.

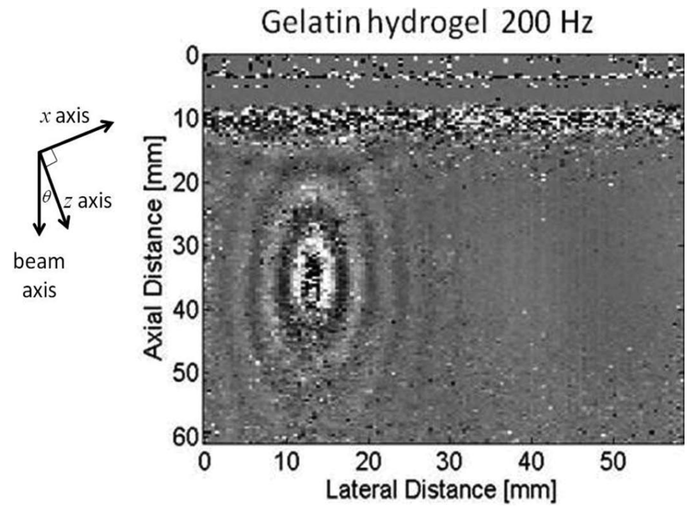

Fig. 2. Particle velocity image $\hat{v}(x\cos\theta, z\cos\theta)$ in gelatin from one RF frame. Shear waves are generated by a needle moving near the elliptical center. The x, z axes (Fig. 1) are rotated $\theta = 30°$ counterclockwise about the needle.

erated echo waveforms with a center frequency of f_c = 6 MHz. Doppler pulse transmission was synchronous with actuator excitation. At each lateral position x, up to 3000 Doppler pulses were emitted at a rate of 10 kHz so the total acquisition time was $T_s \leq 300$ ms. The beam-axis position was shifted laterally 0.46 mm, one array element, after each packet transmission, except near the field edges where the beam was electronically steered. The lateral beam increment was verified using a phantom (ATS Laboratories, model 539). 128 A-lines were recorded per RF frame with beam interpolation turned off. RF echo waveforms were sampled at 40 Msamples/s (fast time) and internally downsampled to 20 Msamples/s.

Typical Doppler velocity estimation is based on pulse-pair phase-shift estimation measurements using lag-one autocorrelation [16]. Acquisition time is divided into M' = 500 records of 0.6 ms, the temporal-phase sampling interval, where $1 \leq m' \leq M'$. Within each record, there is an ensemble of six echoes from $M = 6$ pulse transmissions. The index $1 \leq m \leq M$ counts the echo waveforms in "slow time" sampled on the interval $T_{\text{prf}} = 0.1$ ms within the ensemble. The analytic signal of the echo waveform V and its complex conjugate V^* were entered into the lag-one correlation estimator of temporal phase:

$$\hat{\phi}[\ell, n, m'] = \frac{1}{M-1} \sum_{m''=M(m'-1)+1}^{M(m'-1)+M-1} V^*[\ell, n, m'']V[\ell, n, m''+1]\,. \tag{1}$$

The process was repeated for each of $1 \leq n \leq N$ echo range samples in the A-line range and for the $1 \leq \ell \leq L$ A-lines at lateral indices along the x-axis of the array. Phase estimates are approximately constant with range, and therefore values are averaged spatially over 10 range samples using a running mean:

$$\bar{\phi}[\ell, n', m'] = \sum_{n''=n'}^{n'+10} \hat{\phi}[\ell, n'', m']/10 \quad \text{for } 1 \leq n' \leq N'.$$

From these data, we estimate the instantaneous particle velocity $\hat{v}$ as a function of time and space for each frame of RF data (see Fig. 2) using [17], [18]

$$\hat{v}[\ell, n', m'] = \left(\frac{-c}{4\pi f_c T_{\text{prf}} \cos\theta}\right) \arg(\bar{\phi}[\ell, n', m']), \tag{2}$$

where c is the compressional-wave speed of sound in the medium (1.5 mm/μs) and $\arg(\bar{\phi})$ indicates the phase angle of spatially averaged estimates. High-pass wall filtering is disabled for these acquisitions. $\hat{v}$ estimates the z-axis component of particle velocity where we track the sign of $\arg(\bar{\phi})$ to indicate movement toward or away from the transducer.

Time-harmonic shear wave excitation produces a narrow velocity spectrum, which correlates the echo data within each M-pulse ensemble record. Therefore, we may combine multiple phase lags within the ensemble to improve performance.

B. Lag-k Phase Velocity Estimator

Lag-k estimation of the mean velocity has been investigated by several authors within the weather radar community [19], [20], where it is called poly-pulse-pair processing. This method is able to reduce velocity estimation variance for narrow-band Doppler echoes when the echo SNR is less than 30 dB. The improvement is due to averaging phase estimates whose fluctuations are caused by zero-mean echo-signal noise.

Lag-k estimation is a generalization of (1):

$$\hat{\phi}[\ell, n, m', k] = \frac{1}{M-k} \sum_{m''=M(m'-1)+1}^{M(m'-1)+M-k} V^*[\ell, n, m'']V[\ell, n, m''+k], \tag{3}$$

where P correlation estimates are computed within each M-pulse record such that $1 \le k \le P \le M$. We spatially average estimates along the z-axis and combine the $P = 5$ estimates at a point while eliminating phase-angle ambiguity via

$$\arg(\bar{\phi}[\ell, n', m']) = \frac{1}{10P} \sum_{n''=10(n'-1)+1}^{10(n'-1)+10} \sum_{k=1}^{P} \frac{1}{k} \arg(\hat{\phi}[\ell, n'', m', k]). \tag{4}$$

Choosing $P = 1$ reduces (4) to the lag-one autocorrelation estimate. Eq. (4) estimates may be applied to (2) to find $\hat{v}(t)$ (Fig. 1, left plot), and then further processed to estimate the shear-wave phase speed from estimates of spatial phase (Fig. 1, right plot and Fig. 2), as will be shown later.

The maximum detectable particle velocity $\hat{v}_{\max}$ is limited by the $\pm\pi$ bound on temporal phase. For the lag-one estimate of (1), (2) gives $\hat{v}_{\max} = c/4f_cT_{\mathrm{prf}}$. The disadvantage of the lag-k phase estimate of (4) is the k-fold reduction in $\hat{v}_{\max} = c/4f_cT_{\mathrm{prf}}k$.

C. Rheological Models

Like many soft tissues, gelatin gels can be modeled as linear viscoelastic media. Our goal in this section is to relate observed properties of particle displacement waves to the viscoelastic properties that characterize media in which they travel. Beginning with a solution to the wave equation for elastic solids, we extend the result to include the frequency-dependent complex modulus of viscoelastic media. The results depend on the assumed rheological model describing dynamic behavior of the medium. We then show how temporal phase estimates are applied to the estimation of shear-wave phase speed. The wave speed dependence on applied force frequency, that is, dispersion, is used to estimate the complex modulus.

The Navier wave equation for particle displacement vector $\mathbf{u} = (u_x, u_y, u_z)$ [m] in a homogeneous elastic solid is [21],

$$\rho \frac{\partial^2 \mathbf{u}}{\partial t^2} = (\lambda + \mu)\nabla\nabla \cdot \mathbf{u} + \mu\nabla^2\mathbf{u} + \rho\mathbf{f}. \tag{5}$$

λ and μ are Lamé constants [Pa], ρ is the mass density of the medium [kg/m^3], and $\mathbf{f} = (f_x, f_y, f_z)$ is the external body force per unit mass of the medium [m/s^2]. Let $\mathbf{x} = (x, y, z)$ and $r^2 = x^2 + y^2$.

A needle is inserted into the gel along the z-axis and vibrated harmonically without slipping at radial frequency ω along z with force $\mathbf{f} = (0, 0, f_z(\mathbf{x}, t))$ where $f_z(\mathbf{x}, t) = f_0(r)e^{-i\omega t}$. That force displaces the needle as $\mathbf{u} = (0, 0, u_z(\mathbf{x}, t))$ where $u_z(\mathbf{x}, t) = u_0(r)e^{-i\omega t}$. If the needle length and the medium dimensions are both larger than several wavelengths, we can model the experiment as a source radiating into an infinite homogeneous medium. These shear waves diverge cylindrically from the needle along r, and $f_0(r) = C\mu\delta(r)/\pi\rho r$, where C [m] is a dimensionality constant and $\delta(r)/\pi r = \delta(\mathbf{r}) = \delta(x)\delta(y)$ is the 2-D Dirac delta. Lacking compressional waves, $\nabla \cdot \mathbf{u} = 0$, and (5) reduces to

$$\begin{aligned} -\omega^2 u_z(\mathbf{x}, t) &= \frac{\mu}{\rho} \nabla_r^2 u_z(\mathbf{x}, t) + f_z(\mathbf{x}, t) \\ -k_s'^2 u_0(r) &= \nabla_r^2 u_0(r) + C\delta(r)/\pi r\,, \end{aligned} \tag{6}$$

where the elastic shear-wave number $k'_s = \sqrt{\rho\omega^2/\mu} = \omega/c_s$ for shear-wave speed $c_s = \sqrt{\mu/\rho}$, and $\nabla_r^2 = \partial^2/\partial r^2 + (1/r)(\partial/\partial r)$.

We now solve (6) for u_0, the z component of particle displacement within the x, y plane. Leveraging polar symmetry, a solution is found by taking the Hankel transform of (6) and solving for $U_0(\xi) \triangleq \mathcal{H}u_0(r) = C/(\xi^2 - k_s'^2)$. The inverse transform yields the spatial part of displacement [21],

$$\begin{aligned} u_0(r) = \mathcal{H}^{-1}U_0(\xi) &= \frac{i\pi C}{2} H_0^{(1)}(k'_s r) \\ &\simeq \sqrt{\frac{-\pi C^2}{2k'_s r}} e^{i(k'_s r - \pi/4)}\,. \end{aligned} \tag{7}$$

The exact solution (first form) includes $H_0^{(1)}$, a zeroth-order Hankel function of the first kind. The approximate solution (second form) includes the asymptotic expansion of $H_0^{(1)}$ for large $k'_s r$ [22]. At 50 Hz, $k'_s r \simeq 3$ at 1 cm from the needle.

Applying the correspondence principle [23], [24], we can extend the above solution for linear *elastic* solids to include linear *viscoelastic* solids. To do this, we represent the dynamics of viscoelastic media with a complex shear modulus from the Kelvin-Voigt (KV) rheological model, $\mu = \mu_1 - i\omega\eta$. μ_1 is the elastic shear constant and η is the dynamic viscous constant of the KV model. The wave number for viscoelastic media is now complex, $k_s = \sqrt{\rho\omega^2/\mu} = k'_s + i\alpha_s$, where α_s is the shear-wave attenuation coefficient. Also, shear speed can vary with frequency for the KV model [25]:

$$c_s(\omega) = \omega/\Re\{k_s\} = \sqrt{\frac{2(\mu_1^2 + \omega^2\eta^2)}{\rho(\mu_1 + \sqrt{\mu_1^2 + \omega^2\eta^2})}}$$

and

$$\alpha_s(\omega) = \Im\{k_s\} = \sqrt{\frac{\rho\omega^2(\sqrt{\mu_1^2 + \omega^2\eta^2} - \mu_1)}{2(\mu_1^2 + \omega^2\eta^2)}}. \tag{8}$$

Eq. (8) relates μ_1 and η to measurements of shear wave dispersion [4] and attenuation. Our next step is to estimate c_s from the spatial phase of harmonic shear wave propagation.

D. Shear Speed From Spatial Phase Gradient

The z component of particle velocity is, from (7),

$$v(x,t) = \frac{\partial}{\partial t} u_0(x) e^{-i\omega t} = \sqrt{\frac{\pi\omega^2 C^2}{2k_s x}} e^{i(k_s x - \omega t - \pi/4)} = V_0(x) e^{i\gamma(t)} e^{i\psi(x)} . \tag{9}$$

Because we measure velocity in the x, z plane (Fig. 1), we replace r with x. The last form of the complex velocity expression of (9) separates velocity magnitude $V_0(x)$ from the temporal and spatial phase factors. Because k_s is complex, it requires some algebra to show that the spatial phase gradient is

$$\frac{\mathrm{d}\psi}{\mathrm{d}x} = \frac{\omega}{c_s(\omega)} . \tag{10}$$

Thus c_s is estimated from the spatial phase gradient of particle velocity. In practice, phase is sampled along the x-axis at a constant interval equal to the transducer array pitch, $X = 0.46$ mm, such that $x[\ell] = \ell X$.

Let $\hat{v}'$ be the analytic signal of particle velocity estimates from (2). Recall that we compute as many as 500 temporal velocity estimates at each location in the $x[\ell], z[n']$ image plane. Beginning with the left-most A-line in Fig. 1, we compute a four-sample running mean in space and average 40 values in time (after the transient wave has dissipated) to form spatiotemporally-averaged estimates,

$$\bar{\psi}[\ell', n'] = \frac{1}{40} \sum_{m'=301}^{340} \frac{1}{3} \sum_{\ell''=\ell'}^{\ell'+3} \hat{v}'^*[\ell'', n', m'] \hat{v}'[\ell''+1, n', m']. \tag{11}$$

Phase $\bar{\psi}[\ell', n']$ is a function of space via $x[\ell'], z[n']$.

In the Appendix, we show that $\mathrm{d}\psi/\mathrm{d}x$ from (10) is approximately $(\arg \bar{\psi})/X$. Similar to that found by Hoyt *et al.* [5] for crawling wave imaging, the average shear speed is

$$\hat{c}_s(\omega) = \frac{\omega X}{\langle \arg(\bar{\psi}[\ell', n']) \rangle_{\Omega(\omega)}}, \tag{12}$$

where $\langle \cdot \rangle_{\Omega(\omega)}$ indicates that we further spatially average values over area Ω near the vibrating needle where the velocity SNR > 20 dB. Area Ω includes a subset of indices ℓ', n' that becomes smaller with ω because attenuation increases and needle vibration amplitude decreases with frequency. The standard deviation of $c_s(\omega)$ estimates is found using the number of independent samples within $\Omega(\omega)$ as the degrees of freedom. The number of independent samples was estimated from the 2-D autocovariance function for $\hat{v}(x, z)$.

Analogous to the maximum detectable particle velocity in Section II-A, we can estimate the minimum detectable

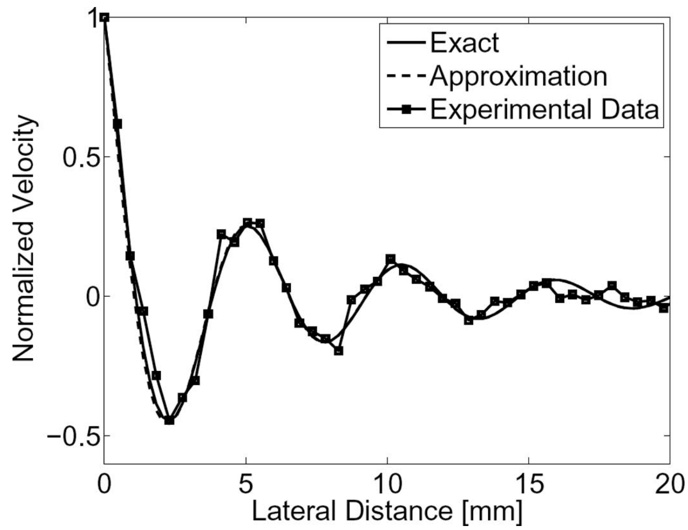

Fig. 3. Comparisons of the exact (solid line) and approximate (dashed line) solutions to the cylindrical wave equation with measured values for 4% gelatin gel (solid-squares line) at $\omega/2\pi = 150$ Hz. Good agreement between the three justifies the phase gradient approach of (12). Note $k_s' x \simeq 1$ at $x = 1$ mm.

shear-wave velocity from the bound on the spatial phase argument: $|\arg(\hat{\psi})| < \pi$. The minimum detectable shear wave velocity from (12) is therefore $\omega X/\pi$.

We close this section by comparing measurements of spatial phase in a gelatin gel with the exact and large-argument approximate predictions in Fig. 3. Clearly the approximation is accurate within measurement error even for $k_s' x = 1$.

E. Complex Modulus From Shear Wave Dispersion

Viscoelastic parameters μ_1 and η are estimated by comparing modeled and measured data using least-squares fitting techniques: predicted values are obtained from (8) and measured values from (12). Assuming measurement errors are normally distributed $\mathcal{N}(0, \sigma^2)$, the maximum-likelihood principle suggests that estimates $\hat{\mu}_1, \hat{\eta}$ are given by the parameters that minimize the sum of weighted, squared residuals,

$$\min \sum_{j=1}^{J} \left(\frac{\hat{c}_s(\omega_j) - c_s(\omega_j; \mu_1, \eta)}{\sigma_j} \right)^2 . \tag{13}$$

There are J frequencies in the bandwidth at 50-Hz intervals. Minimization was performed using a Levenberg-Marquardt method with precalculated analytical gradients [26].

F. Gelatin Gel Samples

Gelatin samples (250 bloom strength, Type B, Rousselot, Buenos Aires, Argentina) were constructed to test the method. Gelatin powder and distilled water are heated in a water bath at a temperature between 65 and 68°C for one hour and periodically stirred. When the sample is cooled to 50°C, formaldehyde is added (0.1% by weight) and thoroughly mixed. We also mixed in cornstarch particles (3% by weight) to introduce random acoustic scatterers. Molten gelatin is poured into cylindrical molds (11.3 cm diameter, 7.5 cm height) and allowed to congeal. Homogenous samples with 4% or 8% w/w gelatin concentrations were tested.

Material properties of the same gelatin gels were tested in a parallel-plate shear rheometer (Model AR-G2, TA Instruments, New Castle, DE) using additional samples. Samples 2.5 cm in diameter and 0.2 to 0.4 cm high were removed from their molds one day after gelation and bonded to the rheometer plates using cyanoacrylate (Rawn America, Spooner, WI). Five percent shear strain was applied. For each of the 4% and 8% gelatin concentrations, five samples were tested and the measured relaxed shear modulus was averaged, giving $\mu_1 = 571 \pm 67$ Pa and 2286 ± 315 Pa, respectively. η cannot be estimated by this method. Although shear modulus increased quadratically with gelatin concentration, no change was detected with the addition of cornstarch particles.

III. Results

A. Phase Estimator Performance

The performance of the lag-k phase estimator ($P = 5$) compared with lag-1 estimator is known to depend on the echo SNR and the correlation between ensemble echoes, i.e., the relative Doppler spectral bandwidth [19], [20]. To help us decide when to apply each estimator, we simulated an ensemble of RF echo signals in one spatial dimension and time so we could measure velocity variances.

Doppler-pulse echo simulations assumed constant particle velocities in the range gate that varied between 0 and 8 cm/s. This range was observed experimentally in gelatin at 100 Hz needle vibration. We modeled scatterers using a white Gaussian random field scanned by a linear time-invariant pulse-echo system with 6-cycle pulses and other parameters given in Section II-A. Zero-mean, additive, white Gaussian noise was added to echoes to adjust the echo SNR.

Estimator performance was quantified from the errors observed using simulated echo data. If $\mathrm{var}(\hat{\upsilon}_1)$ and $\mathrm{var}(\hat{\upsilon}_k)$ are measured variances for the lag-1 and lag-k particle velocity estimates ($M = 6$ for both), the percent improvement for the lag-k estimator relative to lag-1 is given by the factor

$$\xi = 100\left(1 - \sqrt{\frac{\mathrm{var}(\hat{\upsilon}_k)}{\mathrm{var}(\hat{\upsilon}_1)}}\right), \tag{14}$$

which can be positive or negative. The echo simulator was validated by comparing velocity variances measured from simulated data to those predicted [27].

Fig. 4 shows the improvement as a function of the fractional Doppler bandwidth that is normalized by the maximum detectable velocity $2\hat{\upsilon}_{\max}$. This normalized bandwidth is labeled σ_{vn} in Fig. 4. At high echo SNR (40 dB), the lag-k estimator provides advantages only for extremely narrow-band Doppler spectra. At 10 dB echo SNR, however, there is a 60% to 70% improvement at all bandwidths. In the 20 to 30 dB range of echo SNR—the range of greatest experimental interest—the advantage is primarily at low bandwidth. Because of long wavelengths, particle velocity in shear-wave imaging is nearly constant within a range gate. Pulse bandwidth, which has the largest effect on Doppler spectral bandwidth, dictates the relative advantage of lag-k estimation over lag-1.

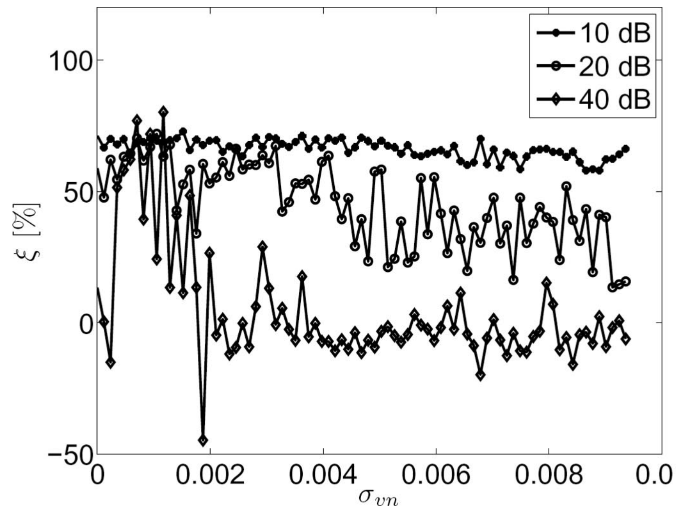

Fig. 4. Percent improvement ξ is plotted as a function of normalized Doppler spectrum width σ_{vn} for 10, 20, and 40 dB echo SNR ratio. Results are from simulated echo data.

We also estimated ξ for experimental data. Shear wave recordings were repeated 19 times for 4% gelatin concentration at 100, 300, and 400 Hz. The improvement factor is plotted in Fig. 5 as a function of lateral distance from the needle source. We find that, although the echo SNR is constant with x, the improvement factor ξ increases with x, suggesting the greatest advantage of lag-k estimation is at low particle velocity (low amplitude shear waves). The advantage stems from the reduction in Doppler bandwidth that accompanies lower mean velocity.

B. Modulus Measurements in Gelatin

Measured shear-wave dispersion curves for 4% and 8% gelatin samples are shown in Fig. 6. For both concentrations, measurements of three gel samples are shown along with best-fit dispersion model curves from (8). Values for μ_1 and η obtained by minimizing (13) are listed in Table I along with mean values ± standard deviation and rheometer estimates of μ_1. Correlation coefficients of the fit, r^2, were computed using the method of Cameron [28] as adapted for our application [29]. The actuator voltage amplitude was 15 V.

Three dispersion measurements and corresponding best-fit model curves are displayed for one 4%-concentra-

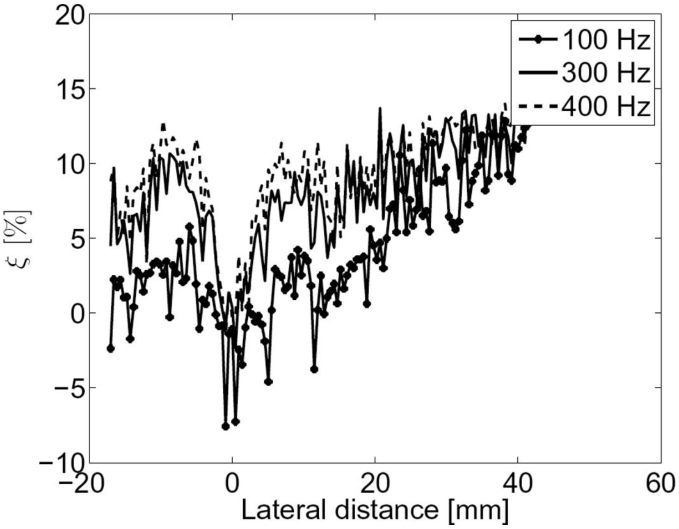

Fig. 5. Percent improvement ξ is plotted as a function of lateral distance from the source for 100, 300, and 400 Hz shear wave frequencies. Results are measured from gelatin gels.

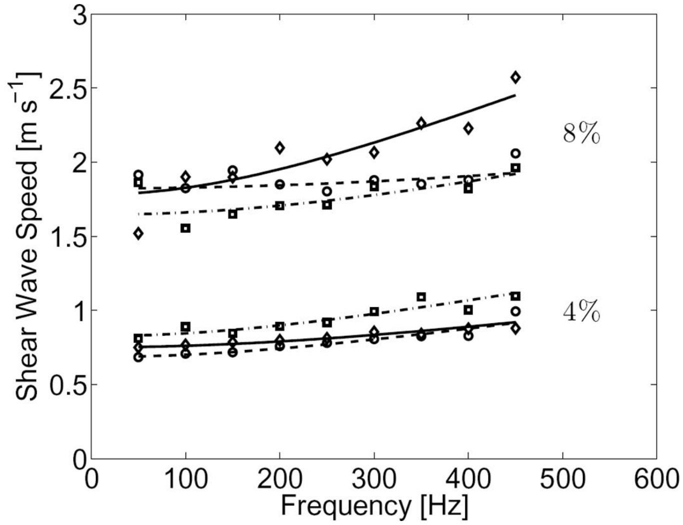

Fig. 6. Measurements of shear wave dispersion in six samples, three each with 4% and 8% gelatin concentration. Lines are best-fit dispersion models used to estimate the complex moduli listed in Table I. For both concentrations, measurements from sample 1 are indicated by a circle, sample 2 by a diamond, and sample 3 by a square.

TABLE I. Viscoelastic Parameter Measurements for Gelatin Gels.

	μ_1 [Pa]	η [Pa s]	r^2
4% Gelatin			
Sample 1	469	0.18	0.87
Sample 2	564	0.17	0.83
Sample 3	680	0.27	0.85
Average	571 ± 105	0.21 ± 0.06	
Rheometer	571 ± 67		
8% Gelatin			
Sample 1	3323	0.47	0.1
Sample 2	3173	0.34	0.8
Sample 2	2708	0.7	0.5
Average	3068 ± 321	0.84 ± 0.45	
Rheometer	2286 ± 315		

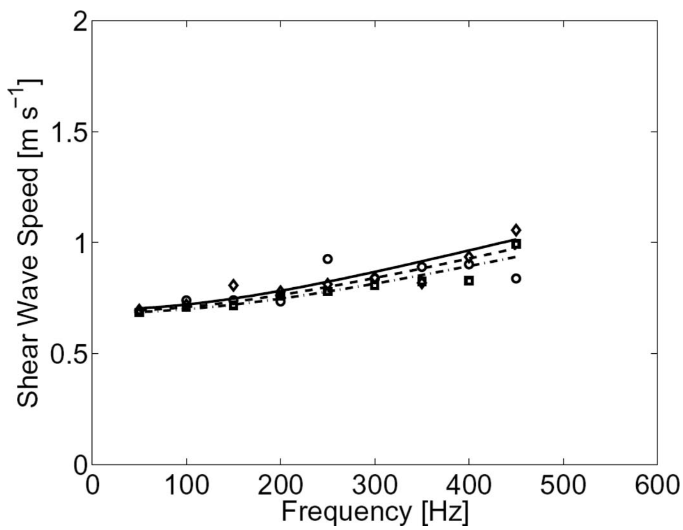

Fig. 7. Measurements of shear wave dispersion in one 4% gelatin sample for actuator voltages set to 5, 10, and 15 V. Lines are best-fit dispersion models used to estimate the complex modulus. Equivalence of the three responses demonstrates the linear mechanical response of the gelatin gel.

tion gelatin sample in Fig. 7. Measurements were acquired for 5, 10, and 15 V mechanical actuator voltage amplitudes that provided three different particle displacements at the needle surface. Particle displacement amplitudes at 50 Hz estimated in gel regions immediately adjacent to the needle gave peak measured displacement amplitudes of $\mu_{5V} = 86$ μm, $\mu_{10V} = 185$ μm, and $\mu_{15V} = 255$ μm. Particle displacement amplitudes at 450 Hz were found to be much smaller $\mu_{5V} = 0.3$ μm, $\mu_{10V} = 0.7$ μm and $\mu_{15V} = 1$ μm. From these data, we estimated μ_1 at 5, 10, and 15 V to be, respectively, 476, 482, and 469 Pa. We also estimated η and found values of, respectively, 0.21, 0.21, and 0.18 Pa·s. Close agreement among estimates at the three applied strains supports the assumption of linearity in gelatin between 50 and 450 Hz.

IV. Discussion

We compared rheometer measurements to shear-wave estimates of μ_1 in the previous section to validate results. Although the two measurements are based on different rheological models, direct comparisons between some parameters are possible [30]. The Maxwell model is often used in the constitutive equation describing shear rheometry. We found a third-order Maxwell model represents rheometer measurements in gelatin [31] with the time-varying shear modulus

$$G(t) = G_0 + G_1 e^{-t/\tau_1} + G_2 e^{-t/\tau_2} + G_3 e^{-t/\tau_3}, \qquad (15)$$

for constants G_i and τ_i. The relaxed modulus of the Maxwell model is G_0, which we obtain at $t \gg \tau_{\max}$ where $G(t$

$\to \infty) \simeq G_0$. Comparing this result with the complex modulus of the KV model in the frequency domain, $\mu(\omega) = \mu_1 - i\omega\eta$, it can be shown that G_0 from rheometry is comparable to μ_1 from shear wave imaging. These values may be compared in Table I. Unfortunately, no similar relationship exists between η and Maxwell model parameters. We compared measurements in fresh and damaged liver tissues with those reported by other labs using different techniques, and we found general agreement for $c_s(\omega)$ [32]. Inter-lab consistency may help validate viscoelastic measurements in complex-structured tissues.

Rheological models help us parameterize the viscoelastic behavior of materials: the Kelvin-Voigt model describes creep; the Maxwell model describes stress relaxation. Of the two, the Kelvin-Voigt model is thought to be more representative of shear wave propagation through gelatin. However, the Zener model (series connection of an elastic spring and a Kelvin-Voigt unit) is the simplest model that predicts both phenomena in linear viscoelastic polymeric solids [33]. We now summarize its frequency response in the context of our analysis.

The complex modulus that results from the Zener model is given by [33]

$$\mu^Z(\omega) = \mu_1 \frac{1+\omega^2\tau_\sigma\tau_\varepsilon}{1+\omega^2\tau_\sigma^2} - i\omega\mu_1 \frac{\tau_\varepsilon - \tau_\sigma}{1+\omega^2\tau_\sigma^2}, \qquad (16)$$

where $\mu_1 = \mu^Z(0)$ is the relaxed modulus and τ_σ and $\tau_\varepsilon \geq \tau_\sigma$ are time constants.

The complex wave number for the Zener model is $k_s^Z = (\rho\omega^2/\mu_Z)^{1/2} = \omega/c_s^Z + i\alpha_s^Z$, which can be expressed in terms of shear wave speed and attenuation coefficient using

$$c_s^{K,Z}(\omega) = \omega/\Re\{k_s^{K,Z}\} = \sqrt{\frac{2\left(\Re\{\mu^{K,Z}\}^2 + \Im\{\mu^{K,Z}\}^2\right)}{\rho\left(\Re\{\mu^{K,Z}\} + \sqrt{\Re\{\mu^{K,Z}\}^2 + \Im\{\mu^{K,Z}\}^2}\right)}}$$

and

$$\alpha_s^{K,Z}(\omega) = \Im\{k_s^{K,Z}\} = \sqrt{\frac{\rho\omega^2\left(\sqrt{\Re\{\mu^{K,Z}\}^2 + \Im\{\mu^{K,Z}\}^2} - \Re\{\mu^{K,Z}\}^2\right)}{2\left(\Re\{\mu^{K,Z}\}^2 + \Im\{\mu^{K,Z}\}^2\right)}}. \qquad (17)$$

K, Z indicates that parameters from either the Kelvin-Voigt or Zener models may be applied.

We estimated parameters of the Zener model for the same gelatin sample data described previously, and we list them in Table II. These may be compared with results from Table I. The small difference between μ_1 results for the KV model in the two tables depends on whether data from three samples were first averaged and then fitted to a model (Table II) or if data from each sample are fitted and μ_1 values averaged (Table I).

Eq. (17) is fitted to the averaged dispersion measurements from 4% and 8% gelatin concentration, and the

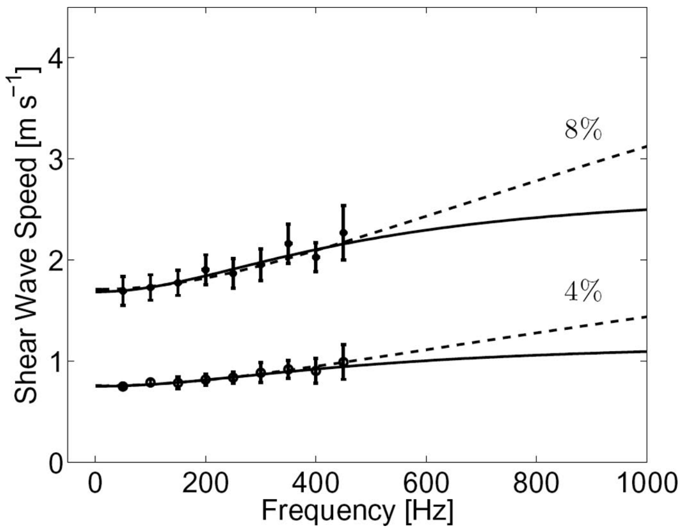

Fig. 8. Average shear-wave dispersion measured for 4% and 8% gelatin concentrations and best-fit model curves. The dashed lines are for the Kelvin-Voigt model and solid lines are for the Zener model. Error bars indicate one standard error based on measurements from three samples each.

TABLE II. Estimated Parameters From Zener (Z) and Kelvin-Voigt (KV) Models are Compared With G_0 From Rheometry in 4% and 8% Gelatin.

Gelatin	μ_1 [Pa]	τ_ε [ms]	τ_σ [ms]
4% Gelatin			
Z	563	0.53	0.2
KV	570		
Rheometer	$G_0 = 571 \pm 67$		
8% Gelatin			
Z	2836	0.53	0.21
KV	2919		
Rheometer	$G_0 = 2286 \pm 315$		

results are shown in Fig. 8. Averaged measurements are also plotted with standard errors indicated. For both models, the shear speed at low frequency is $\sqrt{\mu_1/\rho}$, increasing monotonically with ω. However, the Kelvin-Voigt model is unbounded $c_s(\infty) \to \infty$, whereas the Zener model is bounded by $c_s(\infty) \to \mu_1(\tau_\varepsilon/\tau_\sigma)$. In the 50 to 450 Hz shear-wave bandwidth, the two models agree within measurement uncertainties, and therefore each represents measurement in gelatin gels equally. Only at higher frequencies do the two models diverge. Frequency characteristics of viscous losses have also been quantified using a quality factor $Q(\omega) = -\Re\{k_s^2\}/\Im\{k_s^2\}$ or its inverse Q^{-1} called the dissipation factor [33]. Relaxation peak of the Zener model is located at $f_0 = 1/(2\pi\tau_0)$ where $\tau_0 = \sqrt{\tau_\varepsilon\tau_\sigma}$ and represents a peak of viscous loses. For the estimated properties for 4% and 8% gelatin estimated relaxation peaks are located at $f_0^{4\%} = 503$ Hz and $f_0^{8\%} = 481$ Hz.

V. Conclusion

We have described a method for measuring the complex shear modulus of hydrogel samples. Eventual applications of these measurements include the basic-science goal of following changes in the mechano-environment of 3-D cell cultures undergoing malignant cell transformations and tumor development. More detailed knowledge of cellular mechanobiology on the scale of a millimeter is expected to help illuminate the role of elasticity imaging in cancer diagnosis.

We generated shear waves by vibrating a thin needle along its long axis. This geometry provided closed-form solutions to the shear wave equation that yielded a Green's function describing how wave energy propagates and is dissipated in the surrounding medium. Long needles induce extended and predictable fields of shear waves that yield high velocity SNRs for materials characterization below 450 Hz. We image time-harmonic waves under steady-state conditions to use lag-k estimators of phase, thus improving the reliability of shear-wave dispersion measurements for modulus estimation. Our approach lends itself to accurate estimation of the complex shear modulus parameters. Accuracy of the elastic shear modulus estimates was verified through comparisons with the relaxed modulus from parallel-plate rheometry, where agreement was observed.

The current method is based on an inversion of the shear-wave dispersion equation. One limitation of this method is that measurements at several frequencies must be obtained to estimate each complex modulus value. Furthermore, material homogeneity and reflectionless boundaries are assumed within the measurement region, which is a reasonable assumption for our proposed applications. Therefore the phase-gradient method is an acceptable method for measuring a modulus from velocity estimates.

One alternative approach to needle vibration is to apply an amplitude-modulated acoustic radiation force to a sphere placed in the medium [29], [34], [35]. An oscillating sphere produces shear wave energy that also has known closed-form expressions, and thus permits quantitative mechanical analysis of the medium. However the dipole radiation pattern is more complex and more heterogenous within any Doppler imaging plane. However, radiation force offers the best opportunity for extending the stimulus force frequency above 500 Hz, where clear distinctions among rheological models become more apparent. The displacement amplitude of mechanical actuators mechanically loaded by a needle placed in a viscous gel is significantly reduced at higher frequencies because of the actuator itself or from needle slippage. The SNR for velocity estimates becomes the limiting factor when imaging shear waves above 500 Hz not only because precise force patterns are difficult to generate, but also because of wave divergence and absorption at distances greater than a couple millimeters from the source. We conclude that accurate measurements of the complex shear modulus may be achieved with needle vibration in viscoelastic hydrogels up to 450 Hz.

Appendix

This appendix shows that the model for the spatial phase gradient of shear waves described by (10) is related to lateral estimates of spatial phase from (11) by the equation $\mathrm{d}\psi/\mathrm{d}x \simeq \arg(\hat{\psi})/X$. This discussion follows a derivation by Jensen [17].

The analytic signal for particle velocity as a function of lateral position $\hat{v}'(x)$ is a function of the Hilbert transform of velocity $\hat{v}_h(x)$, namely:

$$\begin{aligned} \hat{v}'(x) &= \hat{v}(x) + i\hat{v}_h(x) \\ &= \sqrt{\hat{v}^2 + \hat{v}_h^2}\, e^{i\tan^{-1}(\hat{v}_h/\hat{v})} = A(x)e^{i\psi(x)}. \end{aligned} \tag{18}$$

Noting explicitly that x is sampled and that $\psi[\ell] \triangleq \psi(x[\ell])$, we have

$$\begin{aligned} \Delta\psi[\ell] &= \psi[\ell+1] - \psi[\ell] \\ &= \tan^{-1}\left(\frac{\hat{v}_h[\ell+1]}{\hat{v}[\ell+1]}\right) - \tan^{-1}\left(\frac{\hat{v}_h[\ell]}{\hat{v}[\ell]}\right). \end{aligned} \tag{19}$$

Using the identity

$$\tan(A-B) = \frac{\tan(A) - \tan(B)}{1 + \tan(A)\tan(B)}, \tag{20}$$

we find

$$\Delta\psi[\ell] = \tan^{-1}\left(\frac{\hat{v}_h[\ell+1]\hat{v}[\ell] - \hat{v}_h[\ell]\hat{v}[\ell+1]}{\hat{v}[\ell+1]\hat{v}[\ell] + \hat{v}_h[\ell]\hat{v}_h[\ell+1]}\right). \tag{21}$$

Turning to measurements, the kernel of the lag-1 correlation estimate without averaging is

$$\begin{aligned} \hat{v}'^*[\ell]\hat{v}'[\ell+1] &= (\hat{v}[\ell] - i\hat{v}_h[\ell])(\hat{v}[\ell+1] + i\hat{v}_h[\ell+1]) \\ &= (\hat{v}[\ell]\hat{v}[\ell+1] + \hat{v}_h[\ell]\hat{v}_h[\ell+1]) \\ &\quad + i(\hat{v}[\ell]\hat{v}_h[\ell+1] - \hat{v}_h[\ell]\hat{v}[\ell+1]). \end{aligned} \tag{22}$$

Thus, we can write

$$\begin{aligned} \arg(\hat{\psi}[\ell]) &= \tan^{-1}\left(\frac{\hat{v}_h[\ell+1]\hat{v}[\ell] - \hat{v}_h[\ell]\hat{v}[\ell+1]}{\hat{v}[\ell+1]\hat{v}[\ell] + \hat{v}_h[\ell]\hat{v}_h[\ell+1]}\right) \\ &= \Delta\psi[\ell], \end{aligned} \tag{23}$$

and finally

$$\frac{\mathrm{d}\psi}{\mathrm{d}x} \simeq \frac{\Delta\psi[\ell]}{X} = \frac{\arg(\hat{\psi}[\ell])}{X} \tag{24}$$

provided $X \ll 2\pi c_s/\omega$.

Acknowledgments

The authors gratefully acknowledge Rousselot Inc., Dubuque, IA, for generously supplying the gelatin; the Autonomic Materials Laboratory and Prof. Sottos at the Beckman Institute for rheometer use; and the Bioacoustics Research Laboratory and Prof. O'Brien at the Beckman Institute for use of their facilities. We gratefully acknowledge the support of Dr. L. Huang and the U.S. Department of Energy through the LANL/LDRD Program for this work. This work was supported in part by the National Cancer Institute under award number R01 CA082497.

References

[1] T. A. Ulrich, A. Jain, K. Tanner, J. L. Mackay, and S. Kumar, “Probing cellular mechanobiology in three-dimensional culture with collagen-agarose matrices,” *Biomaterials*, vol. 31, no. 7, pp. 1875–1884, 2010.

[2] M. Makale, “Cellular mechanobiology and cancer metastasis,” *Birth Defects Res. C Embryo Today*, vol. 81, no. 4, pp. 329–343, 2007.

[3] E. L. Baker and M. H. Zaman, “The biomechanical integrin,” *J. Biomech.*, vol. 43, no. 1, pp. 38–44, 2010.

[4] S. Chen, M. Fatemi, and J. F. Greenleaf, “Quantifying elasticity and viscosity from measurement of shear wave speed dispersion,” *J. Acoust. Soc. Am.*, vol. 115, no. 6, pp. 2781–2785, 2004.

[5] K. Hoyt, K. J. Parker, and D. J. Rubens, “Real-time shear velocity imaging using sonoelastographic techniques,” *Ultrasound Med. Biol.*, vol. 33, no. 7, pp. 1086–1097, 2007.

[6] H. Kanai, “Propagation of vibration caused by electrical excitation in the normal human heart,” *Ultrasound Med. Biol.*, vol. 35, no. 6, pp. 936–948, 2009.

[7] Y. Yamakoshi, J. Sato, and T. Sato, “Ultrasonic imaging of internal vibration of soft tissue under forced vibration,” *IEEE Trans. Ultrason. Ferroelectr. Freq. Control*, vol. 37, no. 1, pp. 45–53, 1990.

[8] R. Muthupillai, D. J. Lomas, P. J. Rossman, J. F. Greenleaf, A. Manduca, and R. L. Ehman, “Magnetic resonance elastography by direct visualization of propagating acoustic strain waves,” *Science*, vol. 269, no. 5232, pp. 1854–1857, Sep. 29, 1995.

[9] S. Chen, M. W. Urban, C. Pislaru, R. Kinnick, Y. Zheng, A. Yao, and J. F. Greenleaf, “Shearwave dispersion ultrasound vibrometry (SDUV) for measuring tissue elasticity and viscosity,” *IEEE Trans. Ultrason. Ferroelectr. Freq. Control*, vol. 56, no. 1, pp. 55–62, 2009.

[10] J. Bercoff, M. Tanter, and M. Fink, “Supersonic shear imaging: A new technique for soft tissue elasticity mapping,” *IEEE Trans. Ultrason. Ferroelectr. Freq. Control*, vol. 51, no. 4, pp. 396–409, Apr. 2004.

[11] H. Kanai, “Propagation of spontaneously actuated pulsive vibration in human heart wall and in vivo viscoelasticity estimation,” *IEEE Trans. Ultrason. Ferroelectr. Freq. Control*, vol. 52, no. 11, pp. 1931–1942, Nov. 2005.

[12] J. Vappou, C. Maleke, and E. E. Konofagou, “Quantitative viscoelastic parameters measured by harmonic motion imaging,” *Phys. Med. Biol.*, vol. 54, no. 11, pp. 3579–3594, 2009.

[13] V. Dutt, R. R. Kinnick, R. Muthupillai, T. E. Oliphant, R. L. Ehman, and J. F. Greenleaf, “Acoustic shear-wave imaging using echo ultrasound compared to magnetic resonance elastography,” *Ultrasound Med. Biol.*, vol. 26, no. 3, pp. 397–403, Mar. 2000.

[14] M. Yin, J. Woollard, X. F. Wang, V. E. Torres, P. C. Harris, C. J. Ward, K. J. Glaser, A. Manduca, and R. L. Ehman, “Quantitative assessment of hepatic fibrosis in an animal model with magnetic resonance elastography,” *Magn. Reson. Med.*, vol. 58, no. 2, pp. 346–353, Aug. 2007.

[15] M. Sridhar and M. F. Insana, “Ultrasonic measurements of breast viscoelasticity,” *Med. Phys.*, vol. 34, no. 12, pp. 4757–4767, 2007.

[16] C. Kasai, K. Namekawa, A. Koyano, and R. Omoto, “Real-time two-dimensional blood flow imaging using an autocorrelation technique,” *IEEE Trans. Sonics Ultrason.*, vol. SU-32, no. 3, pp. 458–463, 1985.

[17] J. A. Jensen, *Estimation Of Blood Velocities Using Ultrasound: A Signal Processing Approach.* New York, NY: Cambridge University Press, 1996.

[18] R. J. Doviak and D. S. Zrnic, *Doppler Radar and Weather Observations.* 3rd ed., San Diego, CA: Academic, 1993.

[19] P. R. Mahapatra and D. S. Zrnic, “Practical aglorithms for mean velocity estimation in pulse Doppler weather radars using a small number of samples,” *IEEE Trans. Geosci. Rem. Sens.*, vol. GE-21, no. 4, pp. 491–501, 1983.

[20] P. T. May, T. Sato, M. Yamamoto, S. Kato, T. Tsuda, and S. Fukao, “Errors in the determination of wind speed by Doppler radar,” *J. Atmos. Ocean Tech.*, vol. 6, no. 2, pp. 235–242, 1984.

[21] K. F. Graff, *Wave Motion in Elastic Solids.* New York, NY: Dover, 1991.

[22] M. Abromowitz and I. A. Stegun, *Handbook of Mathematical Functions.* New York, NY: Dover, 1972.

[23] K. R. Rajagopal and A. S. Wineman, “A quasi-correspondence principle for quasi-linear viscoelastic solids,” *Mech. Time-Depend. Mater.*, vol. 12, no. 1, pp. 1–14, 2008.

[24] L. Khazanovich, “The elastic-viscoelastic correspondence principle for non-homogeneous materials with time translation non-invariant properties,” *Int. J. Solid Struct.*, vol. 45, no. 17, pp. 2–10, 2008.

[25] E. L. Madsen, H. J. Sathoff, and J. A. Zagzebski, “Ultrasonic shear wave properties of soft tissues and tissuelike materials,” *J. Acoust. Soc. Am.*, vol. 74, no. 5, pp. 1346–1355, 1983.

[26] R. C. Aster, B. Borchers, and C. H. Thurber, *Parameter Estimation and Inverse Problems*, Elsevier Academic Press, San Diego, 2005.

[27] C. Kargel, G. Plevnik, B. Trummer, and M. F. Insana, “Doppler ultrasound systems designed for tumor blood flow imaging,” *IEEE Trans. Instrum. Meas.*, vol. 53, no. 2, pp. 524–536, 2004.

[28] A. C. Cameron and F. A. G. Windmeijer, “R-squared measures for count data regression models with applications to health-care utilization,” *J. Bus. Econ. Stat.*, vol. 14, no. 2, pp. 209–220, 1996.

[29] M. Orescanin, K. S. Toohey, and M. F. Insana, “Material properties from acoustic radiation force step response,” *J. Acoust. Soc. Am.*, vol. 125, no. 5, pp. 2928–2936, 2009.

[30] N. W. Tschoegl, *Phenomenological Theory of Linear Viscoelastic Behaviour*, Springer, New York, 1989.

[31] S. Kalyanam, R. D. Yapp, and M. F. Insana, “Poro-viscoelastic behavior of gelatin hydrogels under compression: Implications for bioelasticity imaging,” *ASME J. Biomech. Eng.*, vol. 131, no. 8, art. no. 081005, 2009.

[32] M. Orescanin, M. A. Qayyum, K. S. Toohey, and M. F. Insana, ``Complex shear modulus of thermally-damaged liver,” in *Proc. 2009 IEEE Ultrasonics Symp.*

[33] J. M. Carcione, *Wave Fields in Real Media: Wave Propagation in Anisotropic, Anelastic and Porous Media*, Oxford, UK: Elsevier Science, 2001.

[34] A. B. Karpiouk, S. R. Aglyamov, Y. A. Ilinskii, E. A. Zabolotskaya, and S. Y. Emelianov, “Assessment of shear modulus of tissue using ultrasound radiation force acting on a spherical acoustic inhomogeneity,” *IEEE Trans. Ultrason. Ferroelectr. Freq. Control*, vol. 56, no. 11, pp. 2380–2387, 2009.

[35] S. Chen, M. Fatemi, and J. F. Greenleaf, “Remote measurement of material properties from radiation force induced vibration of an embedded sphere,” *J. Acoust. Soc. Am.*, vol. 112, pp. 884–889, Sep. 2002.

Marko Orescanin received his B.S. degree from the University of Belgrade, Belgrade, Serbia, in 2003 and his M.S. degree from the University of Oklahoma, Norman, in 2005, both in electrical engineering. He is currently working toward his Ph.D. degree in electrical and computer engineering at the University of Illinois at Urbana-Champaign.

His research interests include ultrasonic imaging, pulsed Doppler imaging, remote sensing, and data assimilation.

He received the Spiros G. Geotis Prize in 2006 for his paper “Signal Processing of Beam Multiplexed Data for Phased Array Weather Radar” from the American Meteorological Society. Mr. Orescanin is a student member of IEEE and the IEEE UFFC Society.

Michael F. Insana received his Ph.D. degree in medical physics from the University of Wisconsin–Madison in 1983. His dissertation topic was acoustic scattering and absorption in biological tissues. He was a research physicist at the FDA from 1984 to 1987, where he developed methods for describing tissue microstructure from the statistical properties of echo signals. From 1987 to 1999, he was with the Department of Radiology at the University of Kansas Medical Center. There he directed an imaging research lab that applied ultrasonic imaging to the evaluation of progressive renal failure and breast cancer. Between 1999 and 2004, Mike was Professor of Biomedical Engineering at the University of California, Davis where he directed the graduate program. He is currently Professor and Head of the Department of Bioengineering at the University of Illinois at Urbana-Champaign. His research includes the development of ultrasonic methods for imaging soft tissue microstructure, viscoelasticity, and blood flow. The goal is to understand basic mechanisms of tumor formation and responses to therapy. He is also interested in the principles of imaging system design and performance evaluation, signal processing, detection, and estimation. He is a Fellow of the Acoustical Society of America, the Institute of Physics, and the American Institute of Medical and Biological Engineering. He is also a Senior Member of the IEEE and Associate Editor for *IEEE Transactions on Medical Imaging*.